Naval Research Laboratory

Washington, DC 20375-5320

NRL/MR/5652--09-9194

Analog Photonic Links for Built-in-Testing of Electronic Support Measures (ESM) Systems

JASON D. MCKINNEY
KEITH J. WILLIAMS

Photonics Technology Branch
Optical Sciences Division

CHRISTOPHER SUNDERMAN

Global Strategies Group
Crofton, MD

June 26, 2009

REPORT DOCUMENTATION PAGE

Form Approved
OMB No. 0704-0188

1. REPORT DATE *(DD-MM-YYYY)*	**2. REPORT TYPE**	**3. DATES COVERED** *(From - To)*
26-06-2009	Memorandum Report	01-04-08 – 30-09-2008

4. TITLE AND SUBTITLE

Analog Photonic Links for Built-in-Testing of Electronic Support Measures (ESM) Systems

5a. CONTRACT NUMBER

5b. GRANT NUMBER

5c. PROGRAM ELEMENT NUMBER

6. AUTHOR(S)

Jason D. McKinney, Keith J. Williams, and Christopher Sunderman*

5d. PROJECT NUMBER

5e. TASK NUMBER

5f. WORK UNIT NUMBER

7. PERFORMING ORGANIZATION NAME(S) AND ADDRESS(ES)

Naval Research Laboratory, Code 5650
4555 Overlook Avenue, SW
Washington, DC 20375-5320

8. PERFORMING ORGANIZATION REPORT NUMBER

NRL/MR/5652--09-9194

9. SPONSORING / MONITORING AGENCY NAME(S) AND ADDRESS(ES)

Office of Naval Research
One Liberty Center
875 North Randolph Street
Arlington, VA 22203-1995

10. SPONSOR / MONITOR'S ACRONYM(S)

ONR

11. SPONSOR / MONITOR'S REPORT NUMBER(S)

12. DISTRIBUTION / AVAILABILITY STATEMENT

Approved for public release; distribution is unlimited.

13. SUPPLEMENTARY NOTES

*Global Strategies Group, Crofton, MD

14. ABSTRACT

In this work, we present a photonically enabled built-in-test (BIT) architecture for electronic support measures (ESM) systems. The BIT system employs an analog optical link in concert with a dipole probe antenna and wireless link to provide ~10.5 GHz test signals to the ESM receiver. This work details the optical link design and provides a characterization of the link gain as a function of received photocurrent and photodiode bias. In addition, we describe and characterize the wireless link in terms of the ESM antenna pattern and probe position and polarization. The design of the probe antenna and integrated balun are discussed and gain calibrations are provided. In this work we also provide initial measurements of the impact of the BIT system on receiving operations by measuring the antenna patterns (azimuth and elevation) of the biconical antenna under test. We also discuss extension of the photonic BIT architecture to wideband (500 MHz - 40 GHz) operation.

15. SUBJECT TERMS

Analog photonics
Built-in-test
Electronic support measures

16. SECURITY CLASSIFICATION OF:			**17. LIMITATION OF ABSTRACT**	**18. NUMBER OF PAGES**	**19a. NAME OF RESPONSIBLE PERSON**
a. REPORT	**b. ABSTRACT**	**c. THIS PAGE**			Jason D. McKinney
Unclassified	Unclassified	Unclassified	UL	26	**19b. TELEPHONE NUMBER** *(include area code)* (202) 404-4207

Standard Form 298 (Rev. 8-98)
Prescribed by ANSI Std. Z39.18

CONTENTS

I EXECUTIVE SUMMARY

In this work we present a photonically-enabled built-in-test (BIT) architecture for electronic support measures (ESM) systems. The BIT system employs an analog optical link, in concert with a dipole probe antenna and wireless link, to provide ∼10.5 GHz test signals to the ESM receiver. This work details the optical link design and provides a characterization of the link gain as a function of received photocurrent and photodiode bias. In addition, we describe and characterize the wireless link in terms of the ESM antenna pattern and probe position and polarization. The design of the probe antenna and integrated balun are discussed and gain calibrations are provided. In this work we also provide initial measurements of the impact of the BIT system on receiving operations by measuring the antenna patterns (azimuth and elevation) of the biconical antenna under test. We also discuss extension of the photonic BIT architecture to wideband (∼500 MHz - 40 GHz) operation.

II INTRODUCTION AND MOTIVATION

Intensity-modulated direct-detection (IMDD) radio-frequency (RF) analog optical links are seeing increased use in a variety of commercial and military systems. The diverse range of applications include from radio-over-fiber [1], antenna remoting [2, 3], and optical signal processing [4]. The goal in many of these applications is to perform various "microwave" operations (e.g., amplification) with the photonic link, thereby removing the need for large or power hungry electronic components. These applications have motivated the development of very low noise [5, 6] and highly-linear [7, 8, 9] link architectures. Other applications – such as signal processing [10] and radar applications – [11] benefit greatly from the bandwidth, size, and weight of photonic architectures.

The motivation of the present work is to provide built-in-test capability to existing electronic support measures (ESM) systems – with negligible change (if any) to the existing platform. Analog optical links readily provide the necessary functionality to achieve this capability. In particular, optical links offer very large operation bandwidths, very small form factor and weight, and low power-consumption making them ideal for integration into existing systems. This basic concept of this work is illustrated in Figure 1. For a given ESM platform, a probe antenna is utilized to supply test signals to the receiver via the receiving antenna. Positioned appropriately, the probe will cause inappreciable modifications to the antenna pattern of the receive antenna, while simultaneously enabling a wireless connection to the receiver. An optical link is then utilized to supply the test signals to the probe; collectively, these elements provide an easily-integrated solution for built-in-test capability.

The remainder of this report is structured as follows. In Section III we provide the relevant performance metrics for an analog optical link. The emphasis in this section is placed on the link as an RF / microwave component, described in terms of the user-controlled parameters that determine the link performance. Section IV discusses the implementation of the optical link used in this work and discusses several techniques for altering the link gain (which is the primary metric of interest). In Section V we describe the design of the probe antenna as well as the construction of the probe-to-receiver wireless link. The performance of the built-in-test system is also discussed in this section. In Section VI we provide measurements of the azimuthal and elevation antenna patterns for the biconical antenna in the presence of the BIT system. Section VII summarizes the results to date and system modifications geared to reduce the impact on the ESM antenna patterns and increase the BIT system bandwidth. In the Appendix we provide calibration data for the ESM built-in-test system.

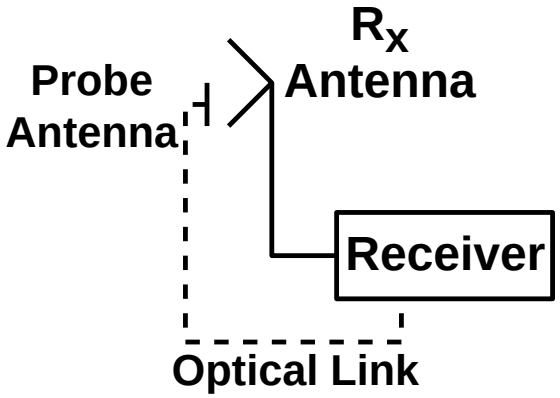

Fig. 1: The photonically-enabled built-in-test concept.

Manuscript approved May 15, 2009.

III INTENSITY-MODULATED DIRECT-DETECTION ANALOG OPTICAL LINKS

The basic theory of operation of analog optical links has been well described in the literature [12, 13]. The purpose of this section is to provide the reader with the primary RF performance metrics for an analog link and to discuss how these may be controlled via several user-defined link parameters. To that end, we will simply state the relevant metrics and leave the derivation of these quantities to the references [12, 14].

The basic externally-modulated analog optical link geometry is shown in Figure 2. The output of a continuous wave laser is modulated with the desired signal via an electrooptic intensity modulator (typically, an integrated lithium-niobate Mach-Zehnder interferometer). The modulated optical signal is then transmitted over some length of optical fiber and the input modulation signal is recovered via a high-speed photodiode. In some link geometries an optical amplifier (erbium-doped fiber amplifiers for systems operating at $\sim$1550 nm) is included either pre- or post modulator for the purpose of increasing the link gain or decreasing the link noise figure [5]. In this work we consider links without optical amplification. For systems employing optical amplifiers, Ref. [13] provides an excellent discussion of the RF performance.

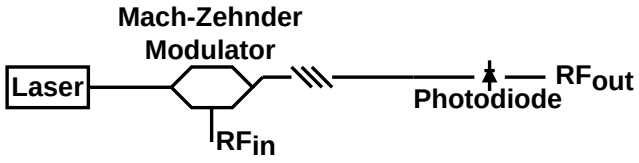

Fig. 2: Intensity-modulated direct detection analog optical link.

If we consider the analog photonic link as an RF "black box", the four primary performance metrics from a system perspective are the gain, noise factor, linear (compression) dynamic range, and spur(ious)-free dynamic range [15]. Ancillary metrics, including the 1-dB compression point and third-order intercept (output), are often utilized as well. The system designer has two basic controls over these metrics: (1) the total optical power (which translates directly to photocurrent, I_{dc}) and (2) The efficiency of the optical modulator, characterized by its halfwave voltage V_π. From a practical perspective, the modulator halfwave voltage (efficiency) is chosen by the designer based on the intended application (more below); because the modulator efficiency is a hardware metric, it is fixed once the modulator is chosen, leaving the photocurrent (optical power) as the primary user-defined control over the link performance.

To begin, we start with the primary difference between an analog optical link and a conventional microwave system – the electrical noise floor. The electrical noise power spectral density (PSD, W/Hz) at the output of an optical link potentially consists of five contributions: input thermal noise (N_{th}) which sees the link RF gain (G_{rf}), output thermal noise generated at the receiver, shot noise generated by the photodetection process, excess laser noise (N_{shot}), and excess noise generated by an optical amplifier (N_{edfa})

$$N_{\text{out}} = N_{\text{th}}\left(\text{G}_{\text{RF}} + 1\right) + N_{\text{shot}} + N_{\text{RIN}} + N_{\text{edfa}}. \tag{1}$$

For an unamplified link, $N_{\text{edfa}} = 0$ and $N_{\text{laser}} = 0$ over the desired frequency range in a well-designed link. For the remainder of this work the amplifier and excess laser noise will be taken to be negligible. For an unamplified link constructed with a low-noise laser, the output noise floor then consists of input and output thermal noise, and shot noise (which corresponds in some sense to the excess noise added by a conventional microwave component). The shot noise contribution to the output noise PSD is given by [16]

$$N_{\text{shot}} = 2qI_{\text{dc}}R_o. \tag{2}$$

Here, q is the magnitude of the electronic charge, R_o is the load resistance seen by the photodiode (taken to be $R_i = 50\ \Omega$ in this work). The received photocurrent I_{dc} is equal to the received optical power P_o multiplied by the responsivity of the photodiode α (A/W). In contrast to the excess noise added by a conventional microwave component, the shot noise level actually varies with the received photocurrent. As we will shortly see, however, the RF gain of the link grows more rapidly with photocurrent than the additional noise. This means for high-gain links the performance will approach that of an input thermal noise-limited system.

Interferometric modulators typically used in RF and microwave analog links are inherently nonlinear devices. The relation between input voltage amplitude and the modulated optical intensity is, in fact, sinusoidal [17]. As a result, the optical modulator is actually the gain compression (saturation) mechanism in the unamplified optical link – we will address this further below. In the small-signal (linear) regime, it can be shown the RF gain of an optical link (for a signal at frequency ω) is given by

$$\text{G}_{\text{RF}} = \left[\pi \frac{I_{\text{dc}}}{V_\pi(\omega)}\right]^2 R_o R_i, \tag{3}$$

where R_i is the input resistance of the optical modulator and R_o is the load resistance seen by the photodiode, and $V_\pi(\omega)$ is the frequency-dependent halfwave voltage of the optical modulator. For this work, both the input and load resistances are taken to be $R_i, R_o = 50\ \Omega$. The RF gain of an analog photonic link is shown, as a function of received photocurrent for several modulator halfwave voltages, in Figure 3 (a). As is clearly seen, the gain increases quadratically with both the photocurrent and the inverse of the modulator halfwave voltage. For a high-gain link then, it is desirable to have a large received photocurrent and a low-V_π (highly-efficient) modulator.

The RF noise factor follows the standard definition [15]

$$\text{nf} = \frac{1}{\text{G}_{\text{rf}}} \frac{N_{\text{out}}}{N_{\text{th}}}. \tag{4}$$

The thermal noise power spectral density $N_{\text{th}} = kT$ (W/Hz), where k is Boltzmann's constant and T = 290 K. Substituting the total output noise PSD [Eq. (1)] into Eq. (4) we obtain the RF noise factor

$$\text{nf} = 1 + \frac{1}{\text{G}_{\text{RF}}} + \frac{1}{\text{G}_{\text{RF}}} \frac{N_{\text{shot}}}{N_{\text{th}}}. \tag{5}$$

The first two terms in this expression for the noise factor correspond to input and output thermal noise, respectively. The last term accounts for the excess noise arising from photodetection. From the expressions for the shot noise PSD [Eq. (2)] and the gain [Eq. (3)], we see this term is inversely proportional to the received photocurrent. This means that, for a large enough gain, the noise factor will approach the input thermal limit of nf $= 1$ [noise figure = NF = 0 dB]. Figure 3 (b) illustrates the link noise figure as a function of photocurrent, again for several modulator halfwave voltages. Note, as the modulator voltage decreases ($V_\pi = 1$ V, e.g.), the link noise figure asymptotically approaches 0 dB for large photocurrents. We should point out, however, single-diode photocurrents are currently limited to $I_{\text{dc}} \sim 100$ mA (research devices – commercial devices are limited to ~25 mA). To significantly exceed this value requires other techniques, such as utilizing photodiode arrays [18].

As mentioned above the compression mechanism in an analog link is the optical modulator. From the nonlinear transfer function of the optical modulator one may solve for the input 1-dB compression point; the resulting input power is given by

$$\text{P}_{\text{1-dB}} = \frac{1}{2} \frac{V_\pi^2}{R_i} \left(\frac{0.9504}{\pi}\right)^2. \tag{6}$$

This input power corresponds to an RF input voltage of $V_{\text{in}} \approx 0.3V_\pi$ (roughly 30% of the modulator halfwave voltage). The range of input powers over which the output signal is above the noise floor, yet below the 1-dB compression point, is the linear (compression) dynamic range given by (W-Hz)

$$\text{LDR} = \text{G}_{\text{RF}} \frac{\text{P}_{\text{1-dB}}}{N_{\text{out}}}. \tag{7}$$

Considering the total output noise given by Eq. (1), in the high-gain limit the dominant noise source is amplified input thermal noise. In this limit we see the LDR approaches a constant value given by $\text{LDR} = P_{\text{1-dB}} / (kT)$. This reveals the trade-off inherent in the choice of optical modulator – highly-efficient (low-V_π) modulators enable high link gain, however, these modulators also limit the LDR as illustrated in Figure 3 (c).

The dominant distortion in an IMDD link utilizing a quadrature-biased Mach-Zehnder modulator link is a third-order nonlinearity arising from the transfer function of the optical modulator. The output third-order intercept point for a two-tone excitation may be derived from the RF response of the modulator and is given by (W)

$$\text{OIP}_3 = 4I_{\text{dc}}^2 R_o. \tag{8}$$

The spur(ious)-free dynamic range – the range of input (or output) powers over which the fundamental output signal is greater than the output noise power and the dominant distortion is less than or equal to the output noise power – is defined as (W-Hz$^{2/3}$)

$$\text{SFDR}_3 = \left(\frac{\text{OIP}_3}{N_{\text{out}}} \right)^{2/3}. \tag{9}$$

Here, N_{out} is given by Eq. (1). From Figure 3 (d), we see the SFDR generally increases with increasing photocurrent. For highly-efficient modulators, however, we again see the dynamic range approaches a constant value given by $\text{SFDR} = 4\left(V_\pi^2/R_i\right) / \left(\pi^2 kT\right)$ in the input thermal noise operational limit. So, while a highly-efficient (low-V_π) optical modulator provides the largest link gain and lowest noise figure (for fixed DC photocurrent) this may not be the best choice for receiver applications requiring high dynamic range (linear or spur-free). A thorough discussion of the trade-offs inherent in the gain, noise figure, and spur-free dynamic range of an analog link is given in [19].

The particular application will obviously determine which metrics are most critical. For example when utilizing an analog link in receiver applications the spur-free dynamic range may be most critical, especially in systems where an RF preamplifier may be used. For transmitter applications where the output photodiode is used to drive an antenna (as in this work) the RF gain and noise figure (potentially linear dynamic range) would be most critical in determining the range of transmitter output powers. In the following section we will discuss the use of an analog link as the RF feed for a probe antenna geared to provide built-in-test capability for ESM platforms. We will primarily focus on the link gain as this is the most relevant performance metric for the application.

IV OPTICAL LINK DESIGN FOR ESM BUILT-IN-TEST APPLICATIONS

In our application, an analog link is used to remote an RF / microwave test signal to a probe antenna placed in close proximity to the antenna of an ESM receiver. For this type of application it is the bandwidth, size and weight of an analog link which is appealing. Because the application does not require that large RF powers be coupled into the receiver, significant flexibility exists in the link design and novel techniques may be employed to modify the link gain (the primary performance metric in this work).

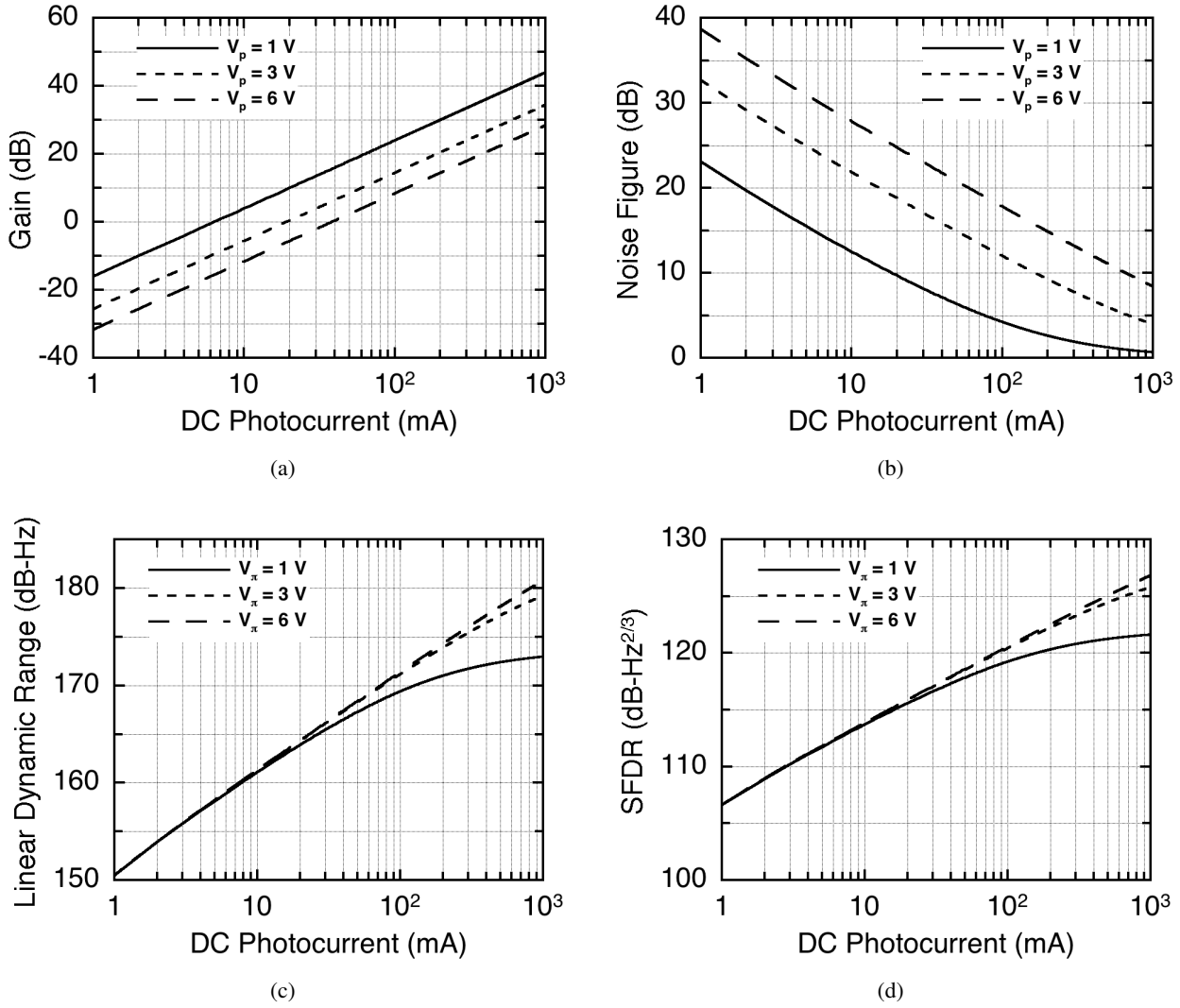

Fig. 3: Primary performance metrics for an analog optical link. (a) RF Gain. (b) RF noise figure. (c) Compression dynamic range. (d) Spurious-free dynamic range. The noise figure, compression- and spurious free dynamic range calculations assume $N_{\text{RIN}} = 0$ and $N_{\text{edfa}} = 0$ in Eq. (1).

The optical link utilized in this work (refer to Fig. 2) employs a commercial telecommunications-grade optical modulator (JDS Uniphase) with a halfwave voltage of $V_\pi = 5.8$ V at 1 GHz ($V_\pi \sim 7.1$ V at 10.5 GHz) and an electrical bandwidth of 15 GHz. The photodiode is a PIN device (Discovery Semiconductor, DSC50S) with a $\sim$12 GHz electrical bandwidth. The link is designed to operate with a maximum DC photocurrent of $I_{\text{dc}} = 10$ mA, which is readily achieved using commercial semiconductor distributed feedback (DFB) lasers.

Effects of Photocurrent, Photodiode Bias Voltage, and Optical Power on the Gain of an Analog Optical Link

At a photocurrent of 10 mA, the nominal link gain at 10.5 GHz [using Eq. (3) with a 6-dB correction to account for the internal matching resistor used in the photodiode] is approximately $G_{rf} = -19$ dB. The measured link gain ($G_{rf} \approx -18$ dB) shown by the solid line in Figure 4 agrees extremely well with the theoretical value expected for 10 mA of received photocurrent. As described in Section III, the gain may be adjusted by changing the DC photocurrent (optical power utilized in the link). To illustrate this, the DC photocurrent is decreased to $I_{dc} = 1$ mA and the measured gain (dashed line) exhibits the expected 20 dB decrease, reaching a value of $G_{rf} \sim -37.5$ dB at 10 GHz. For applications where it is desirable to probe receiver sensitivity, the DC photocurrent provides one simple control variable over the RF gain of the optical link.

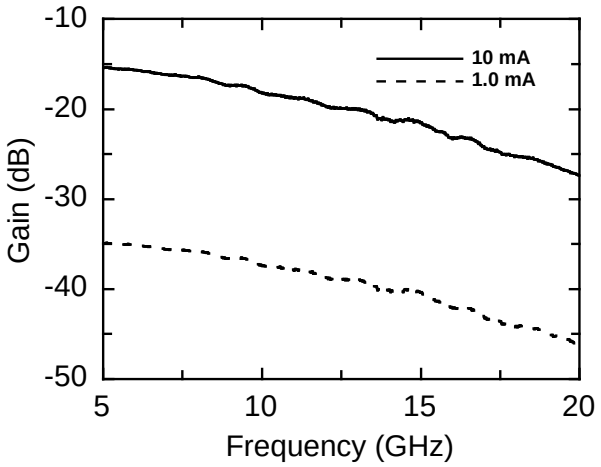

Fig. 4: Measured RF gain ($V_\pi \sim 7.1$ V, $V_{bias} = 5$ V).

A second method of tuning the link gain through changes in the bias voltage of the photodiode. Is is well known that the photodiode functions as a varactor (variable capacitor) with a capacitance controlled by the bias voltage and incident optical intensity [20, 21]. Because the photodiode bandwidth is essentially RC-limited, changes in capacitance directly affect the frequency response of the device. For frequencies near the 3-dB bandwidth of the diode this provides a sensitive method for controlling the link gain. For frequencies well away inside the diode bandwidth, saturation effects decrease the diode DC responsivity which also decreases the link gain. Through these effects, the bias voltage may be used to control the gain in an optical link (either continuous or discrete modifications).

To illustrate the efficacy of this technique we operate the optical link at a received photocurrent of 1 mA and vary the applied bias over the range of $-5 \leq V_{bias} \leq 0$ V while measuring the link gain. Figure 5 shows the variation in link gain with the photodiode bias voltage. The dependence of the photodiode capacitance on bias voltage is readily seen by comparing the link response at the extremes of 5 GHz and 20 GHz. At 5 GHz, the total gain variation from $V_{bias} = -5$ V to $V_{bias} = 0$ V is approximately $\Delta G_{rf} = -6$ dB (determined primarily by saturation of the photodiode). At 20 GHz (which is $\sim$2x higher than the device bandwidth under normal operating conditions) the gain is found to vary over $\Delta G_{rf} \approx -12$ dB for the same change in photodiode bias voltage; this large difference is due to the increase in diode capacitance with decreasing bias voltage.. By examining the gain at 10 GHz [Fig. 5 (b)] we see that the gain slowly degrades

with photodiode biases in the range of $-5 \leq V_{\text{bias}} \leq -1$ V. As the bias voltage decreases below 1 V, the magnitude of the electric field arising from space-charge readily exceeds that of the bias field (opposite polarity), leading to a rapid decrease in diode responsivity (saturation) and link gain.

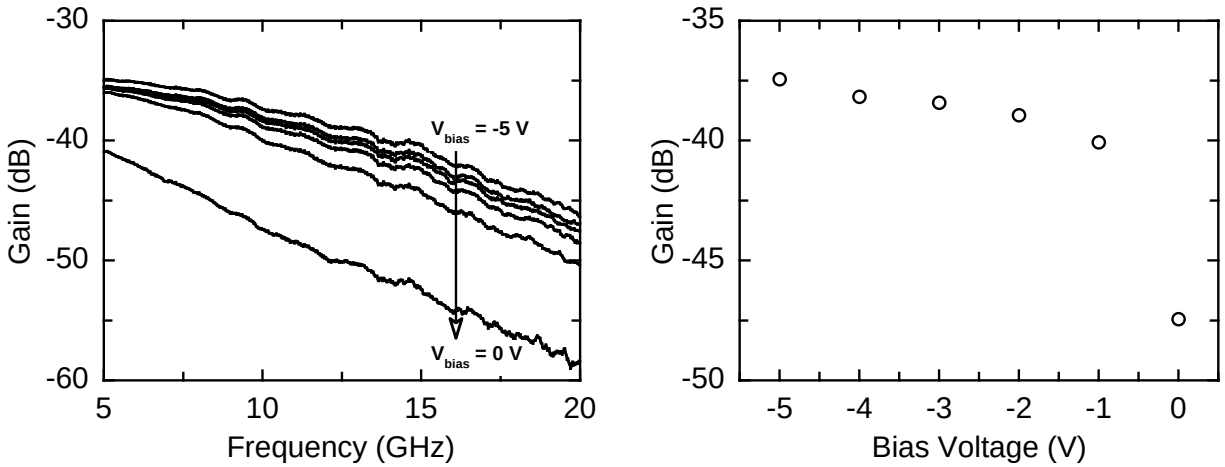

(a) (b)

Fig. 5: (a) Variation in RF gain with photodiode bias. (b) RF gain at 10 GHz as a function of photodiode bias. In both measurements $I_{\text{dc}} = 1.0$ mA

If the photodiode is operated unbiased [bottom curve in Fig. 5 (a)], the incident optical power may also be utilized to vary the link gain. We note, the derivation of the relationship between incident optical power and link gain is beyond the scope of the present work; treatment of the RF response of unbiased photodiodes is given in [22]. Figure 6 shows the link gain at 10 GHz as a function optical power incident on the photodiode. Here, the RF gain is maximized for an optical power of $\sim$1 mW. Below 1 mW, the link gain will vary with the square of the photocurrent, as in Eq. (3). For powers above 1 mW, space-charge screening rapidly leads to collapse of the built-in electric field and a rapid decrease in photodiode response and, consequently, link gain.

As this section shows, the RF gain may be tuned over a user-defined range by varying the optical power in the link and / or the photodiode bias voltage. For applications computer controlled optical attenuators and power supplies may be utilized to provide simple turn-key RF gain control. While the link gain is of primary importance for this application, we provide the all of the calculated performance metrics in Table 1. Here, the calculations are performed using Eqs. (1)–(9) and assume a DC photocurrent of $I_{\text{dc}} = 10$ mA, a modulator halfwave voltage of $V_\pi = 7.1$ V, and that the link is unamplified ($N_{\text{edfa}} = 0$) with no excess laser noise ($N_{\text{RIN}} = 0$).

We note for short optical links the primary instability is the modulator bias voltage. Though not shown explicitly here, the RF gain varies as $\text{G}_{\text{rf}} \propto \sin^2(\phi_{\text{bias}})$, where the bias phase is related to the applied bias voltage (V_{bias}) and the DC halfwave voltage ($V_{\pi,\text{dc}}$) by

$$\phi_{\text{bias}} = \pi \frac{V_{\text{bias}}}{V_{\pi,\text{dc}}}. \tag{10}$$

While the bias voltage (phase) will drift, inexpensive control electronics capable of maintaining the bias phase to within 1° of the desired value are readily available. For a bias phase deviation of $\Delta\phi_{\text{bias}} = 1^\circ$

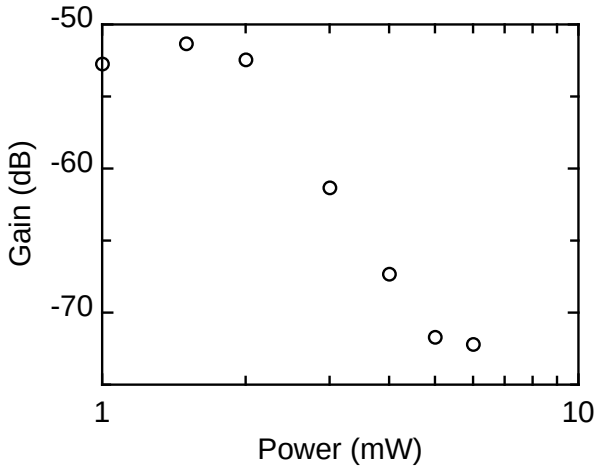

Fig. 6: RF gain as a function of optical power for $V_{\text{bias}} = 0$ V.

Table 1: Analog optical link performance metrics at 10 GHz. ($I_{\text{dc}} = 10$ mA, $V_\pi = 7.1$ V)

Metric	Value
G_{rf} (dB)	-19
NF_{rf} (dB)	29
LDR (dB-Hz)	166
$SFDR_3$ (dB-$Hz^{2/3}$)	118

(from quadrature $\phi_{\text{bias}} = 90^\circ$), the RF gain penalty is $\Delta G_{rf} \approx 1 \times 10^{-3}$ dB – this represents negligible change in RF power.

V PROBE ANTENNA DESIGN AND BIT SYSTEM ARCHITECTURE

In this work, the ESM system of interest utilizes a series of biconical antennas [23] – the basic biconical geometry is shown in Figure 7. The electric and magnetic fields radiated (or received) by the biconical antenna are similar to those for the infinitesimal dipole [24]; for a $\hat{z}$-oriented antenna, the electric and magnetic field polarizations are well described by $\mathbf{E} = E_\theta\hat{\theta}$ and $\mathbf{H} = H_\phi\hat{\phi}$, respectively. Here, E_θ and H_ϕ are the electric (V/m) and magnetic (A/m) field intensities and $\hat{\theta}$ and $\hat{\phi}$ are unit vectors in the θ and ϕ directions. In the far-field these fields appear to be those of a linearly-polarized uniform plane wave with the electric field polarized along the vertical axis of the of the antenna; for the geometry shown in Fig. 7, the electric field would be given by $\mathbf{E} = E_z\hat{z}$ in the far field.

Polarization Dependence

In the system of interest, the biconical antenna is surrounded by a (nominally) -45° linear polarizer. This allows provides a certain amount of (linear) polarization diversity. In Cartesian coordinates we may model

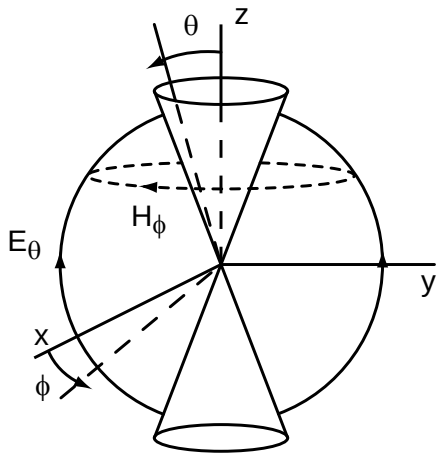

(a)

Fig. 7: Biconical antenna.

a polarizer as a linear spatial filter with an electric field transfer function given by ($\hat{x}$ and $\hat{z}$ are unit vectors in the x and z directions)

$$\mathbf{LP} = \left(\cos\gamma_{\rm p}\,\hat{x} + \sin\gamma_{\rm p}\,\hat{z}\right), \tag{11}$$

where $\gamma_{\rm p} = -45^\circ$ is the angle of the polarizer transmission axis, defined to be positive relative to the positive x-axis in the $x-z$ plane. For an electric field (field strength E_o)

$$\mathbf{E} = E_o\left(\cos\gamma\,\hat{x} + \sin\gamma\hat{z}\right) \tag{12}$$

incident on the polarizer, we see the transmitted field amplitude is given by [$(\cdot)$ denotes the scalar product]

$$\mathbf{E}_{\rm t} = (\mathbf{E}\cdot\mathbf{LP})\,\mathbf{LP} = \cos(\gamma-\gamma_p)\left(\cos\gamma_{\rm p}\,\hat{x} + \sin\gamma_{\rm p}\,\hat{z}\right). \tag{13}$$

For a $\hat{z}$ oriented biconical antenna, the received power is then proportional to $|\mathbf{E}_{\rm t}\cdot\hat{z}|^2$,

$$P_{\rm rx} = P_o\sin^2\!\left(\gamma_{\rm p}\right)\cos^2(\gamma-\gamma_p), \tag{14}$$

where P_o is the power density incident on the polarizer. We see Eq. (14) is simply Malus' Law governing the power transmitted through a linear polarizer (the multiplicative term $\sin\gamma_{\rm p}$ accounts for the orientation of the antenna relative to the polarizer axis) [25].

Probe Antenna Design

Given the application requires only linear polarization, the halfwave dipole is an ideal candidate for the probe antenna in our system. To simplify antenna construction (and positioning requirements) we choose a planar dipole geometry. We choose to operate at 10.5 GHz for our proof-of-concept experiments, therefore the dipole is chosen to be $\sim$1.5 cm in total length (approximately one-half wavelength at 10.5 GHz). We utilize commercially-available packaged photodiodes with a coaxial output in this work. Therefore, to successfully feed the planar dipole antenna (fed by a coplanar stripline), we integrate the antenna with a simple planar Marchand balun [26]. This balun provides a sufficiently low return loss at the design frequency; we note

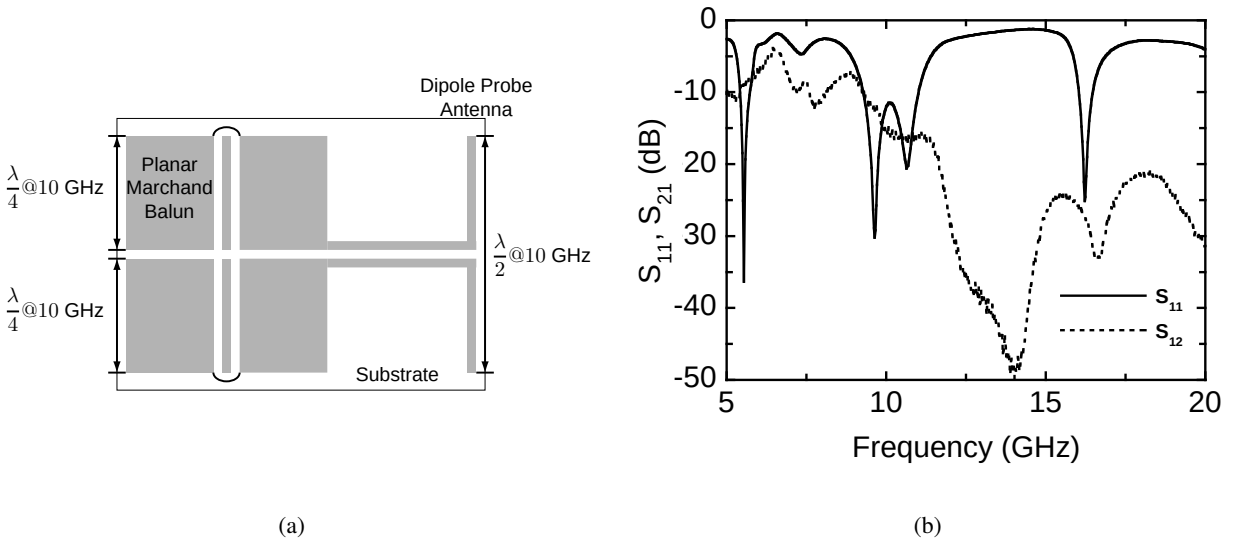

(a) (b)

Fig. 8: (a) 10 GHz dipole antenna (probe) and integrated Marchand balun. (b) Measured power reflection coefficient (S_{11}) for the dipole probe and integrated balun (solid line) and transmission coefficient (S_{21}, dashed line) for two back-to-back Marchand baluns.

the bandwidth may be extended by including additional impedance tapers to ideally match the coplanar-waveguide and stripline impedances [15, 27, 28]. A schematic of the probe antenna is shown in Figure 8 (a) – the footprint of the integrated balun / probe antenna is approximately 4.5 cm^2. The measured return loss (S_{11}, solid line) for the entire probe geometry and the power transmission (S_{21}, dashed line) of two back-to-back baluns are shown in Fig. 8 (b). The measured return loss is below -10 dB in the range of 9.5 – 11 GHz, which agrees well with the balun design. The transmission coefficient shows significant loss at 10 GHz which is attributed to the substrate material (FR4) and non-optimal connector-to-transmission line transitions; both of these loss mechanisms may be readily addressed in future designs and have negligible impact relative to the application addressed here.

Polarization Measurements

Given the structure of the particular ESM platform of interest it is desirable to mount the probe antenna in the horizontal plane ($x - y$ plane in Fig. 7) near the base of the biconical antenna. In this orientation, the probe antenna radiates an electric field orthogonally polarized to that received by the biconical antenna without the polarizer. To verify this probe position supplies adequate signal to the receiver with the polarizer in place, we measure the received power as a function of incident polarization. The measurement geometry is illustrated in Figure 8 (a). In this measurement, the received power at 10 GHz is measured as the probe antenna is rotated relative to the biconical antenna in ($\sim 5^\circ$ steps).

The received power (normalized to its peak value) versus polarization angle is shown in Fig. 8 (b). As expected, the received power is maximized when the probe antenna and polarizer transmission axis are aligned [see Eq. (14)]; a deep null (nominally 15 dB) occurs when the polarizer transmission axis and dipole are orthogonal. For reference, the gray line is Eq. (14) normalized to its peak value for a polarizer transmission axis of $\sim -30^\circ$. As this measurement demonstrates, there is only a 3-dB relative penalty for utilizing horizontal polarization. In terms of absolute power, the $\sim 30^\circ$ offset between the polarizer

transmission axis and biconical antenna orientation yields an overall attenuation of ∼1/4 (-6 dB). As a note, for applications requiring only low-level signals at the receiver virtually any probe orientation may be utilized subject to the particular platform design.

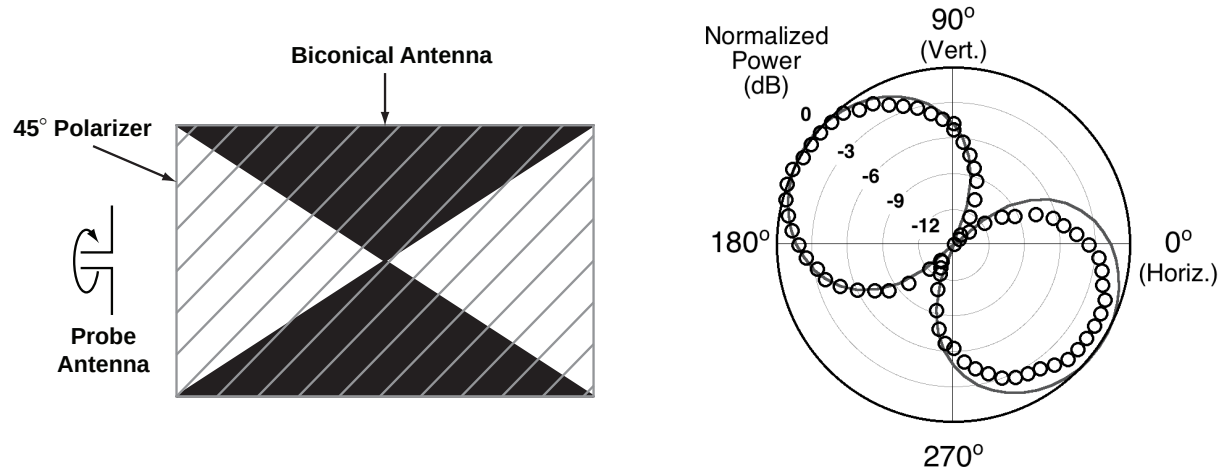

(a) (b)

Fig. 9: (a) Experimental schematic for measurement of polarization dependence. (b) Received power as a function of probe antenna angle [0° referenced to horizontal ($\hat{x}$) polarization].

Wireless Link and Composite BIT System Gain

To estimate the gain of the wireless link shown schematically in Figure 10 (a) (no optics) we must consider the radiation patterns of both the probe dipole and the biconical antenna. We note, the probe antenna is positioned roughly at the boundary between the near and far-field regimes. Therefore, the far-field calculations presented here only provide an estimate of the wireless link gain.

In the far-field region, the normalized radiation pattern (which we will take to be synonymous with the gain for these approximate calculations) of the vertically-oriented large-angle biconical antenna is given by [29, 30]

$$G_{\rm bc} = \sin^2(\theta)\,, \tag{15}$$

where θ is the elevation angle (defined from vertical). Because the probe dipole is oriented orthogonally to the biconical antenna, its radiation pattern in uniform in the elevation plane and is taken to exhibit the maximum gain for a halfwave dipole, $G_{\rm d}$=1.64 (∼2dB) [31].

From the Friis transmission equation (here, including the effects of the polarizer and insertion loss of the probe antenna $L_{\rm p}$)

$$G_{\rm link} = \frac{P_{\rm r}}{P_{\rm t}} = \left(\frac{\lambda}{4\pi R}\right)^2 G_{\rm bc} G_{\rm d} \times \left[\sin^2(\gamma_{\rm p})\cos^2(\gamma - \gamma_p)\right] \times L_{\rm p} \tag{16}$$

we may then calculate the gain of the wireless link. Here, R is the transmission distance from the feedpoint of the biconical antenna to the probe antenna (R = 5.5 cm) and λ = 2.86 cm is the freespace wavelength at 10.5 GHz. Given the probe is positioned at an elevation of $\theta \approx 110^\circ$, the measured polarizer transmission

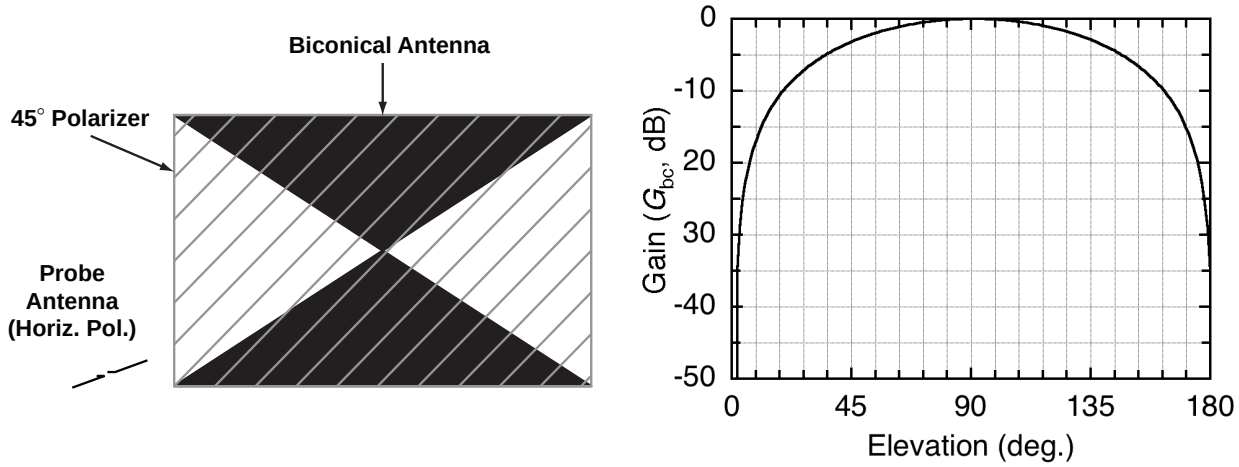

(a) (b)

Fig. 10: (a) Probe antenna location and orientation. The probe antenna polarization is horizontal and the antenna is positioned at an elevation of nominally$\sim 110^\circ$ (from vertical). (b) Approximate gain of the biconical antenna versus elevation angle (θ in Fig. 7).

axis is $\gamma_p \approx -30^\circ$, and that the probe electric field is horizontally-polarized ($\gamma - \gamma_p \approx -30^\circ$) the predicted wireless link gain from Eq. (16) [with L_p $\sim$-12 dB from Fig. 8 (b)] is approximately $G_\mathrm{link} = -45$ dB.

The measured wireless link gain is shown by the solid gray curve in Figure 11. Note, the return loss of the probe antenna is repeated here (dashed gray line) to emphasize the frequency range where this analysis applies. The measured gain of G_link $\approx$-41 dB at 10.5 GHz agrees extremely well with the calculated value of $G_\mathrm{link} = -45$ dB. Here, the primary cause for the discrepancy is the assumption of unity peak gain for the biconical antenna. These antennas typically exhibit a gain of $0 \leq G_\mathrm{bc} \leq 3$ dB, which readily accounts for the difference in calculated and measured wireless link gain. Additionally, the assumed loss of the probe antenna structure ($L_\mathrm{p} = -12$ dB) attributes half of the loss measured for the back-to-back baluns to each individual balun; this may overestimate the loss of the probe structure. The increase in wireless link gain below $\sim$7 GHz is attributed to near-field coupling between the probe and biconical antennas (the far-field approximation is not satisfied for frequencies in this range). The wireless link gain in this frequency range is stable and may be utilized for testing purposes; however, the gain is not readily calculated in the near-field – a calibration of the gain in this range must be experimentally determined. The gain of the composite BIT system (shown by the solid black line in Fig. 11) is determined by the product of the optical link gain and the wireless link gain [Eqs. (3) and (16)]. For reference, the optical link gain (for $I_\mathrm{dc} = 10$ mA) is shown in Fig. 11 by the dashed black line. For a DC photocurrent of $I_\mathrm{dc} = 10$ mA the theoretical gain is $G_\mathrm{BIT} \approx -64$ dB, which agrees very well with the measured value of $G_\mathrm{BIT} \approx -60$ dB at 10.5 GHz.

From a systems perspective, the photonically-enabled BIT capability demonstrated here is geared to provide low-level test signals in theater. With a fixed-power oscillator this system is capable of delivering user-defined power levels to the ESM receiver. For example, with a 1 mW (0 dBm) source the system will provide variable-power signals up to a maximum power level of P_out $\approx$-60 dBm. Incorporation of a higher-power laser or more efficient (low-V_π) modulator could increase the maximum power by over 20 dB.

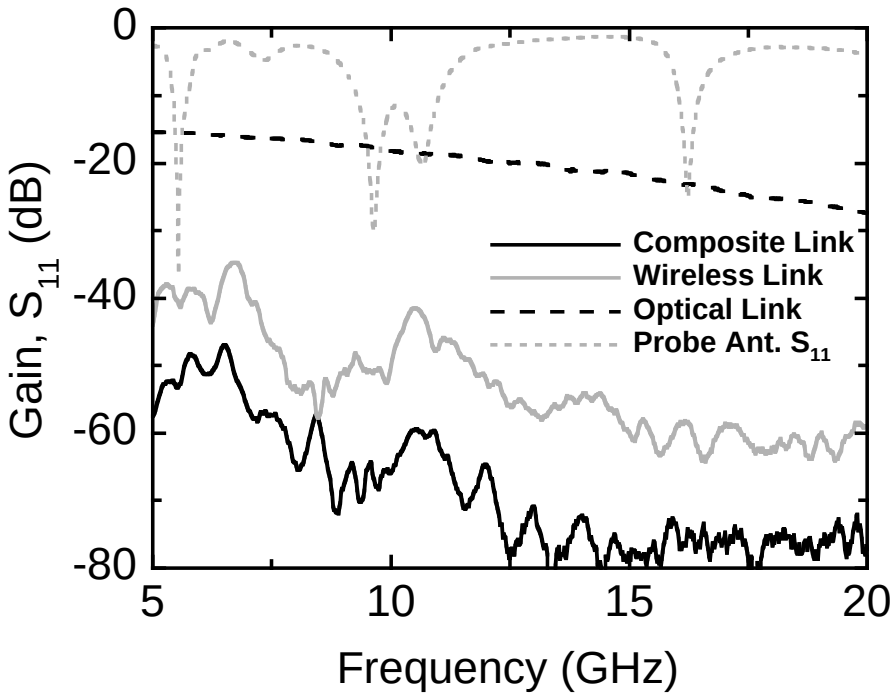

Fig. 11: Measured reflection and transmission patterns for the BIT system. Dashed gray line: probe antenna / balun power reflection coefficient (S_{11}); dashed black line: optical link RF gain (G_{rf}, from Fig. 4 with $I_{dc} = 10$ mA); solid gray line: wireless link gain (G_{link}, no optics); composite wireless link gain (G_{BIT}, wireless+optics).

VI EFFECTS OF THE PHOTONIC BIT SYSTEM ON THE BICONICAL ANTENNA RADIATION PATTERNS

In order for the photonic BIT system to find real-world application, BIT capability must be provided without serious degradation in the ESM system performance This means, the ESM platform antenna patterns must not be adversely affected by the presence of the probe antenna and photodiode. To quantify the effect of the BIT system, we perform far-field measurements of the azimuthal and elevation directivity patterns of the biconical antenna. Figure 12 illustrates the antenna orientation for these measurements; the probe antenna and photodiode are positioned at angular locations AZ = $\sim 0^\circ$ and $\sim 270^\circ$, respectively. We perform one azimuthal and two elevation measurements [one in the plane containing the probe antenna (solid line in Fig. 12) and one in the plane containing the photodiode (dashed line in Fig. 12)] for each polarization over a frequency range spanning the X- and Ku-bands (8.2–12.4 GHz, 100 MHz steps). Note, vertical polarization corresponds to an electric field vector aligned with the vertical axis of the biconical antenna ($\hat{z}$ direction in Fig. 7). For practical reasons, these measurements were performed without the radome in place; however, to justify this, the azimuthal gain was measured both with and without the radome. Though not shown, the only significant difference between the two measurements was a slight uniform decrease in gain ($\lesssim 1$ dB) with the radome in place.

Figure 13 shows the measured azimuthal directivity patterns at center frequencies of 10, 14, and 18 GHz (black line, dark gray line, and light gray line, respectively). For vertically-polarized excitation [Fig. 13 (a)], we see an approximately 5 dB global variation in the directivity at 10 GHz. In the range of approximately

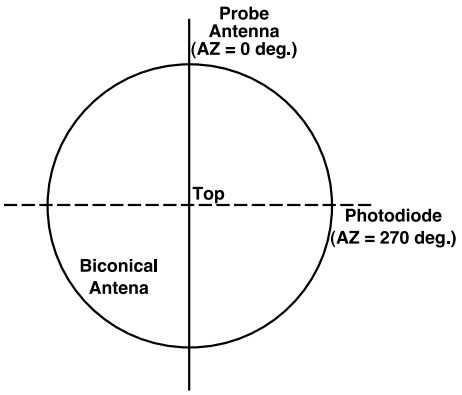

Fig. 12: Schematic of the biconical antenna with the installed BIT system, as observed from above.

$-45^\circ\,(315^\circ) \leq$ AZ $\leq 45^\circ$, the $\sim \pm 1$ dB ripple is attributed to the probe antenna which is designed to be resonant at $\sim$10.5 GHz. Though the probe antenna is horizontally oriented, energy reflected from the nominally 45° polarizer will possess a horizontal field component; this field component will scatter efficiently from the probe. Consistent with this description, the variation in directivity decreases as the excitation frequency is increased away from the probe antenna resonance; the maximum directivity variation is $\sim$2 dB at 14 GHz ($\sim \pm 0.5$ – 0.75 dB ripple) and the ripple decreases to approximately $\pm$0.5 dB at 18 GHz. For comparison, the roughly $\pm$0.5 dB ripple in directivity (at 10 GHz, significantly less at higher frequencies) in the region diametrically opposed to the probe antenna represents the inherent pattern non-uniformity of the biconical antenna as situated in the ESM platform. The resonant feature appearing at AZ $\sim 270^\circ$ is is attributed to scattering from the photodiode bias lines, which run vertically along the outside of the platform below the biconical antenna – these bias lines readily couple to the vertical incident wave. This conclusion is supported by the absence of this feature in the case of horizontally-polarized excitation [Fig. 13 (b)]. We note, this feature may be removed by either re-routing the photodiode bias lines or operating the photodiode in a photo-voltaic (unbiased) mode. Either solution would provide adequate gain for BIT operations.

For horizontally-polarized excitation [Fig. 13 (a), 10 GHz: black line, 14 GHz: dark gray line, 18 GHz: light gray line], the measured patterns show the same general trend. At 10 GHz, the global variation in directivity is approximately 6 dB and the maximum ripple is on the order of $\pm$2 dB. It should be noted that, globally, the measured directivity is on the order of 2 dB lower in the region of the probe antenna (AZ $=\sim 30^\circ$) as compared to the region without the probe (AZ $=\sim 210^\circ$). The pattern ripple increases (for roughly the same global change in directivity) because the excitation field polarization and probe antenna orientation are aligned. The incident field then scatters directly from the probe (without reflection from the polarizer) with the result that the scattered field amplitude is larger than for vertically-polarized excitation. Again, variations in directivity significantly decrease in the region away from the probe antenna and the resonant feature attributed to the photodiode bias lines is absent.

While the azimuthal directivity most clearly shows the effects of the the BIT system, it is also useful to verify the elevation patterns show the same general trends. To illustrate, the elevation patterns in the probe antenna plane (shown by the solid line in Fig. 12) are provided in Figure 14 (a) (vertical polarization) and Figure 14 (b) (horizontal polarization), again at frequencies of 10, 14, and 18 GHz (black, dark gray, and light gray lines, respectively). Elevation patterns in the photodiode plane (dashed line in Fig. 12) are shown for vertical polarization in Fig. 14 (c) and horizontal polarization in Fig. 14 (d) [the excitation frequencies and color scheme are the same as in (a) and (b)]. In all plots, the top of the biconical antenna corresponds to

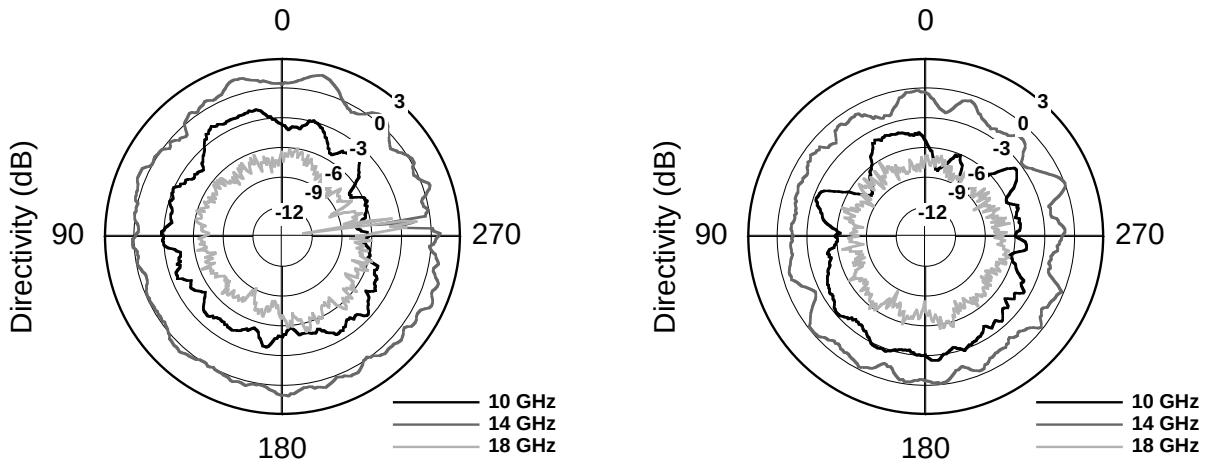

Fig. 13: Azimuthal directivity patterns. (a) Vertical polarization. (b) Horizontal polarization.

an angular position of 0°.

In the plane containing the probe antenna (positioned at an angular location of 270°), the most noticeable feature is that the peak directivity (gain) is approximately 1-2 dB lower in the region of the probe, as compared to the diametrically-opposed region (90°). At 10 GHz the decrease in gain in the probe region is $\Delta G \sim -2$ dB, at 14 GHz $\Delta G \sim -2.5$ dB, and at 18 GHz $\Delta G \sim -1$ dB. In the case of horizontally-polarized excitation, the measured directivity shows a similar trend – for all frequencies the gain in the region of the probe antenna is ~ 2 dB below that of the opposing lobe.

In the photodiode plane, the effects of the BIT system on the elevation pattern are negligible. The most obvious feature is an approximately 3 dB decrease in gain at 10 GHz for vertically-polarized excitation [Fig. 14 (c)] at the location of the photodiode (90°). This feature is a another manifestation of the ripple observed in the azimuthal directivity patterns. We note, from observation of the azimuthal pattern of Fig. 13 (a), the decrease in gain near the photodiode is much broader (angularly) at 10 GHz than at higher frequencies. Thus, it is not surprising there is no decrease in gain observed in the elevation patterns at 14 and 18 GHz – the measured elevation pattern is likely taken at a plane slightly offset from the null locations in Fig. 13 (a). For horizontally-polarized excitation, there is no substantial difference in directivity between the lobes with and without the photodiode, which agrees well with the measured azimuthal pattern of Fig. 13 (b).

VII SUMMARY AND FUTURE WORK

In this work we demonstrate that analog optical links, in concert with a short distance wireless link, may be used to provide built-in-test (BIT) functionality for electronic support measures (ESM) systems. The system presented here utilizes a small dipole probe antenna to provide user-defined signals in the power range of $P_{\text{out}} \lesssim -60$ dBm and at a frequency of $\sim$10.5 GHz to the ESM receiver. The system bandwidth may be extended to span from ultra-high-frequency ($\sim$300 MHz) to the millimeter frequency range ($>$40 GHz) with proper choice of antenna and balun designs. Additionally, multiple probe antennas and / or multiple optical links may be employed to probe different receiver elements. Photonically-enabled BIT systems, by virtue of their small size and low power consumption, may be readily applied to virtually any ESM platform – with

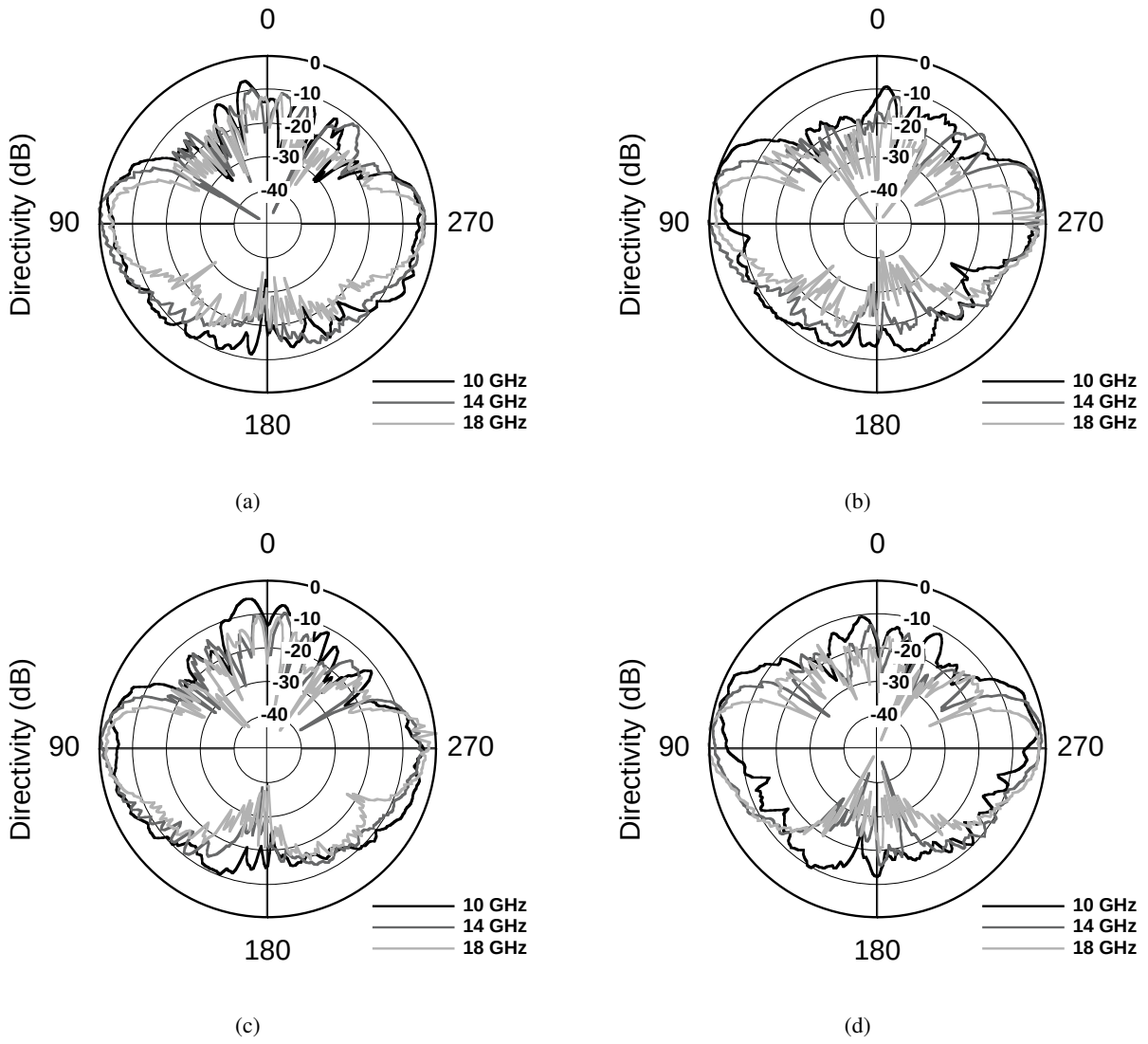

Fig. 14: Elevation directivity patterns. (a) Probe antenna plane, vertical polarization. (b) Probe antenna plane, horizontal polarization. (c) Photodiode plane, vertical polarization. (d) Photodiode plane, horizontal polarization.

negligible change to the existing architecture.

Future work should focus primarily on quantifying (and minimizing) the effects of the probe antenna on receiving operations. Based on the results of our initial directivity measurements, the probe antenna / photodiode geometry does impact the antenna pattern. Directivity variations (ripple) are seen to increase from approximately ± 0.5 dB up to roughly ± 2 dB in the azimuth plane, depending on the frequency and polarization of interest. The probe antenna itself impacts the directivity most significantly; as the wireless link gain is not of primary importance, future designs could employ an electrically-small non-resonant probe antenna to mitigate the observed pattern distortion (with acceptable decreases in wireless link gain). Additionally, integrated photodiodes may be employed to further reduce the BIT system cross-section. The primary factor impacting the BIT system bandwidth is the photodiode utilized in the photonic link; secondary to this is are the antenna and balun bandwidth. By employing broadband photodiodes (up to 60 GHz devices are com-

mercially available) and wideband baluns, the operational bandwidth may be readily extended to beyond 40 GHz.

VIII ACKNOWLEDGEMENT

The authors would like to thank John Valenzi, W. Mark Dorsey, and Mark Parent of the Radar Division, U.S. Naval Research Laboratory, for performing the antenna pattern measurements.

IX REFERENCES

[1] H. Pfrommer, M. A. Piqueras, J. Herrera, V. Polo, A. Martinez, S. Karlsson, O. Kjebon, R. Schatz, Y. Yu, T. Tsegaye, C. P. Liu, C. H. Chuang, A. Enard, F. V. Dijk, A. J. Seeds, and J. Marti, "Full-duplex docsis/wireless docsis fiber-radio network employing packaged afpm-based base-stations," *IEEE Photon. Technol. Lett.*, vol. 18, no. 2, pp. 406–408, January 2006.

[2] V. J. Urick, J. F. Diehl, A. S. Hastings, C. Sunderman, J. D. McKinney, P. S. Devgan, J. L. Dexter, and K. J. Williams, "Analysis of fiber-optic links for hf antenna remoting," U.S. Naval Research Laboratory, NRL Memorandum Report NRL/MR/5650-08-09101, March 2008.

[3] V. J. Urick, A. S. Hastings, J. L. Dexter, K. J. Williams, C. Sunderman, J. F. Diehl, and K. R. Colladay, "Field test on the feasibility of remoting hf antennas with fiber optics," U.S. Naval Research Laboratory, NRL Memorandum Report NRL/MR/5652–08-9137, July 2008.

[4] J. Campany, B. Ortega, D. Pastor, and S. Sales, "Discrete-time optical processing of microwave signals," *J. Lightwave Technol.*, vol. 23, no. 2, pp. 702–723, Feb. 2005.

[5] J. D. McKinney, M. Godinez, V. J. Urick, S. Thaniyavarn, W. Charczenko, and K. J. Williams, "Sub-10 db noise figure in a multiple-ghz analog optical link," *IEEE Photon. Technol. Lett.*, vol. 19, pp. 465–467, April 2007.

[6] H. V. Roussell, M. D. Regan, J. L. Prince, C. H. Cox, J. X. Chen, W. K. Burns, G. E. Betts, E. I. Ackerman, and J. C. Campbell, "Gain, noise figure and bandwidth-limited dynamic range of a low-biased external modulation link," in *2007 IEEE International Topical Meeting on Microwave Photonics*, Oct. 3–5 2007, pp. 84–87.

[7] J. A. MacDonald, M. V. Kuback, and A. Katz, "Wideband dynamic range improvement in microwave photonic links," in *IEEE Avionics, Fiber-Optics and Photonics Conference (AVFOP)*, no. ThB3, Minneapolis, MN,, Sept. 20–22 2005.

[8] B. M. Haas and T. E. Murphy, "A simple, linearized, phase-modulated analog optical transmission system," *IEEE Photon. Technol. Lett.*, vol. 19, no. 10, pp. 729–731, May 2007.

[9] J. D. McKinney, K. Colladay, and K. J. Williams, "Linearization of phase-modulated analog optical links employing interferometric demodulation," *accepted for publication in the IEEE J. Lightwave Technol.*, 2008.

[10] R. A. Minasian, "Photonic signal processing of microwave signals," *IEEE Trans. Microwave Theory Tech.*, vol. 54, no. 2, pp. 832–846, Feb. 2006.

[11] S. Tonda-Goldstein, D. Dolfi, A. Monsterleet, S. Formont, J. Chazelas, and J. Huignard, "Optical signal processing in radar systems," *IEEE Trans. Microwave Theory Tech.*, vol. 54, no. 2, pp. 847–853, 2006.

[12] C. H. Cox III, *Analog Optical Links: Theory and Practice*. New York: Cambridge University Press, 2004.

[13] V. J. Urick, M. S. Rogge, F. Bucholtz, and K. J. Williams, "The performance of analog photonic links employing highly compressed erbium-doped fiber amplifiers," *IEEE Trans. Microwave Theory Tech.*, vol. 54, no. 7, pp. 3141–3145, July 2006.

[14] V. J. Urick, "Long-haul analog photonics principles with applications," Ph.D. dissertation, George Mason University, Fairfax, VA, 2007.

[15] D. M. Pozar, *Microwave Engineering*, 3rd ed. Hoboken: John Wiley and Sons, Inc., 2005.

[16] A. Yariv, *Optical Electronics*, 3rd ed. New York: Holt, Rinehart and Winston, Inc., 1985.

[17] B. E. A. Saleh and M. C. Teich, *Fundamentals of Photonics*. New York: John Wiley & Sons, Inc, 1991.

[18] A. Hastings, V. J. Urick, C. Sunderman, J. Diehl, J. D. McKinney, D. Tulchinsky, P. S. Devgan, and K. J. Williams, "Suppression of even-order photodiode nonlinearities in multi-octave photonic links," *accepted for publication in the IEEE J. Lightwave Technol.*, 2008.

[19] F. Bucholtz, V. J. Urick, M. Godinez, and K. J. Williams, "Graphical approach for evaluating performance limitations in externally modulated analog photonic links," *IEEE Trans. Microwave Theory Tech.*, vol. 56, no. 1, pp. 242–247, Jan. 2008.

[20] K. J. Williams, R. D. Esman, and M. Dagenais, "Nonlinearities in pin microwave photodetectors," *J. Lightwave Technol.*, vol. 14, no. 1, pp. 84–96, Jan. 1996.

[21] S. A. Malyshev and A. L. Chizh, "P-I-N photodiodes for optical control of microwave circuits," *IEEE J. Select. Topics Quantum Electron.*, vol. 10, no. 4, pp. 679–685, Jul./Aug. 2004.

[22] M. E. Godinez, C. S. McDermitt, A. S. Hastings, M. G. Parent, and F. Bucholtz, "RF characterization of zero-biased photodiodes," *J. Lightwave Technol.*, in press 2008.

[23] J. D. Kraus, *Antennas*, 2nd ed. New York: McGraw-Hill, 1988.

[24] C. A. Balanis, *Antenna Theory Analysis and Design*, 2nd ed. New York: John Wiley & Sons, Inc, 1997.

[25] E. Hecht, *Optics*, 2nd ed. Reading: Addison-Wesley, 1987.

[26] W. K. Roberts, "A new wide-band balun," *Proc. IRE*, vol. 45, pp. 1628–1631, Dec. 1957.

[27] R. K. Hoffmann, *Handbook of Microwave Integrated Circuits*. Boston: Artech House, Inc., 1987.

[28] S. Kim, S. Jeong, Y. Kim, J. Lim, K. Seo, and S. Nam, "Ultra-wideband (from dc to 110 GHz cpw to cps transition," *Electron. Lett.*, vol. 38, no. 3, pp. 622–623, June 2002.

[29] C. H. Papas and R. King, "Radiation from wide-angle conical antennas fed by a coaxial line," *Proc. IRE*, vol. 39, pp. 49–51, 1951.

[30] S. N. Samaddar and E. L. Mokole, "Biconical antennas with unequal cone angles," *IEEE Trans. Antennas Propagat.*, vol. 46, no. 2, pp. 181–193, 1998.

[31] S. Ramo, J. R. Whinnery, and T. Van Duzer, *Fields and Waves in Communication Electronics*, 3rd ed. New York: John Wiley and Sons, Inc., 1994.

APPENDIX A

X GAIN CALIBRATION

The purpose of this Appendix is to provide the calibration for the BIT system gain. While we have shown several operating regimes in which the gain may be varied via the optical power (DC photocurrent) and photodiode bias, we focus here on two operating modes: (1) the photodiode bias is held constant at $V_{\text{bias}} = 5$ V and the gain is adjusted via the photocurrent; and (2) The received optical power is held constant at $\sim$1 mW (approximately $I_{\text{dc}} = 1$ mA) and the photodiode bias is utilized to adjust the system gain.

(1) To obtain the BIT system gain in terms of the DC photocurrent we cascade the expressions for the optical link (G_{rf}) and wireless link (G_{link}) gains [Eqs. (3) and (16) in Sections III and V, respectively]. The result is the overall gain of the BIT system,

$$G_{\text{BIT}}(I_{\text{dc}}) = \frac{1}{4}\left(\pi \frac{I_{\text{dc}}}{V_\pi}\right)^2 R_o R_i \times \left(\frac{\lambda}{4\pi R}\right)^2 \sin^2(\theta) \times 1.64 \times \left[\sin^2\left(\gamma_{\text{p}}\right)\cos^2(\gamma - \gamma_p)\right] \times L_{\text{p}} \times C. \quad (17)$$

Here, C is a measured constant that accounts for the difference calculated and measured gain. The factor of $1/4$ accounts for the fact that the analog link employs a photodiode with an internal matching resistor (the maximum power transfer theorem) and 1.64 is the maximum gain for a half-wave dipole. The analog and wireless link parameters for the current system are complied in Table 2. The gain

Table 2: Gain calibration parameters.

Symbol	Quantity	Value
I_{dc}	DC Photocurrent	0.1 – 10 mA
V_π	Halfwave Voltage	7.1 V
R_i	Modulator Resistance	50 Ω
R_o	Load Resistance	50 Ω
λ	Wavelength	2.86 cm (10.5 GHz)
R	Antenna Separation	5.5 cm
θ	Probe Elevation	110°
γ_p	Polarizer Trans. Axis	-30∘
γ	Probe Polarization	0°
L_{p}	Probe Excess Loss	$10^{-1.2}$
C	Gain Correction	$10^{0.4}$

calibration curve for the system, using the DC photocurrent as the gain control mechanism, is shown in Figure 15.

(2) When the photodiode bias is utilized as a gain control mechanism, the gain of the analog optical link is not readily expressed analytically. Because of this, we use a fourth-order polynomial fit to the log-scale data presented in Figure 5 (b). Here, the photodiode current (optical power) is held fixed at

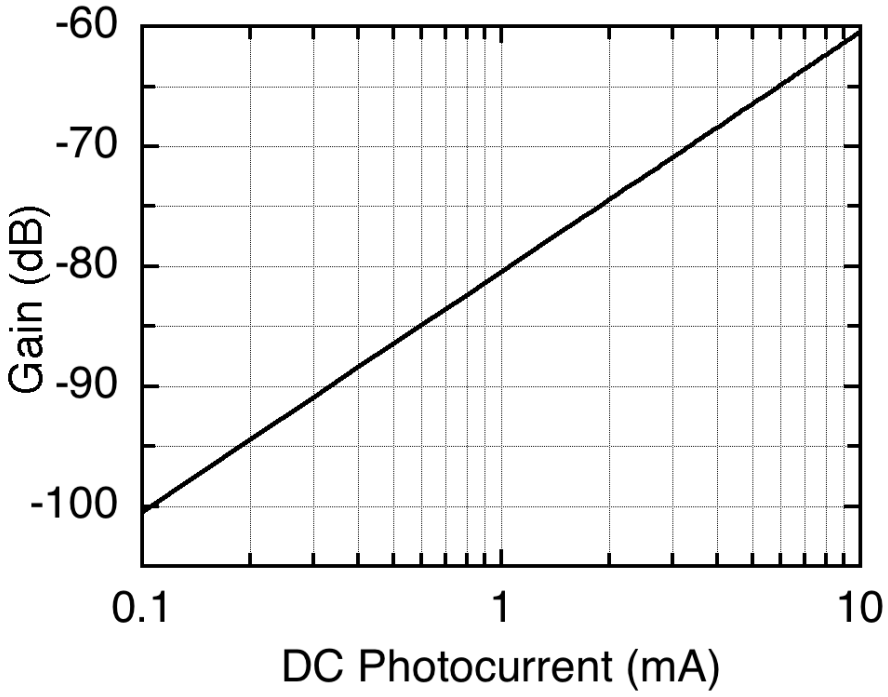

Fig. 15: BIT system gain as a function of DC photocurrent (photodiode bias is held at V_{bias}).

$I_{\text{dc}} = 1$ mA ($P_{\text{opt}} \sim 1$ mW) and the diode bias varies between -5 V and 0 V. With this experimentally-determined optical link gain, the system gain is obtained adding the log-scale gain of the wireless link. The system gain is given by

$$G_{\text{BIT}}(V_{\text{bias}})|_{\text{dB}} = \left[a_0 + a_1 V_{\text{bias}} + a_2 V_{\text{bias}}^2 + a_3 V_{\text{bias}}^3 + a_4 V_{\text{bias}}^4\right] + 10\log\left[\left(\frac{\lambda}{4\pi R}\right)^2 \sin^2(\theta) \times 1.64 \times \left[\sin^2\left(\gamma_{\text{p}}\right)\cos^2(\gamma - \gamma_p)\right] \times L_{\text{p}} \times C\right]. \quad (18)$$

Here, the wireless link parameters are the same as above and are tabulated in Table 2. The polynomial coefficients for the optical link gain are given in Table 3. The calibration curve for the system, as a function of photodiode bias for a fixed photocurrent ($I_{\text{dc}} = 1$ mA) is shown in Figure 16.

Table 3: Coefficients for BIT gain versus photodiode bias voltage.

Coefficient	Value
a_0	-47.42000 (dB)
a_1	-12.19700 (dB/V)
a_2	-6.19720 (dB/V^1)
a_3	-1.34190 (dB/V^3)
a_4	-0.10212 (dB/V^4)

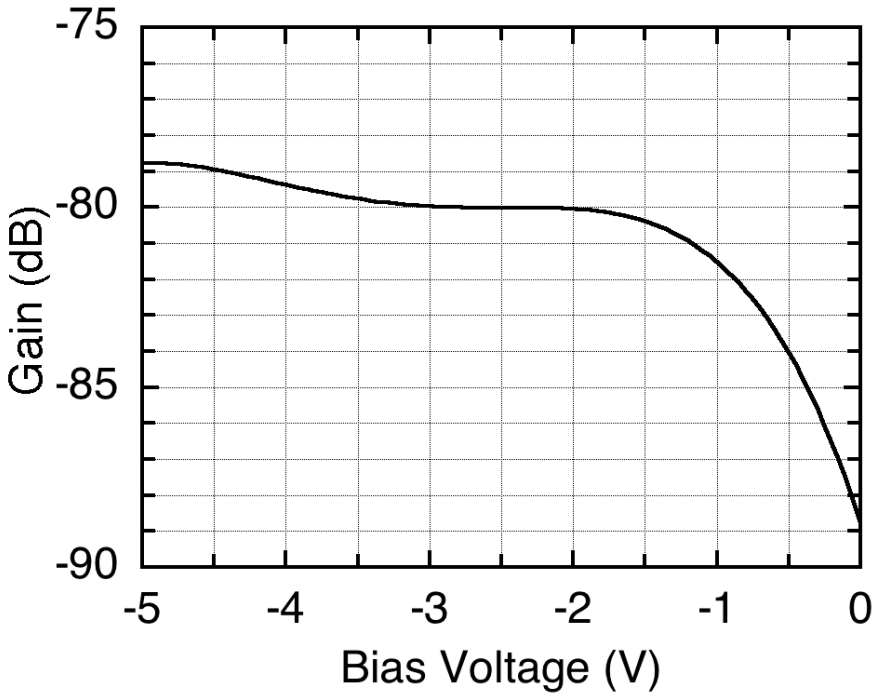

Fig. 16: BIT system gain as a function of photodiode bias ($I_{\text{dc}} = 1$ mA).